Conformation of a Bound Inhibitor of Blood Coagulant Factor Xa†

Daniel R. Studelska,‡,§ Lynda M. McDowell,‡ Marc Adler,|| Robert D. O'Connor,‡ Anil K. Mehta,‡ William J. Guilford,|| Jerry L. Dallas,|| Damian Arnaiz,|| David R. Light,|| and Jacob Schaefer*,‡

Department of Chemistry, Washington University, St. Louis, Missouri 63130, and Berlex Biosciences, 2600 Hilltop Drive, Richmond, California 94804

Received December 17, 2002; Revised Manuscript Received April 7, 2003

ABSTRACT: $^{13}C\{^{15}N\}$ and $^{13}C\{^{19}F\}$ rotational-echo double-resonance NMR have been used to characterize the enzyme-bound structure of ZK-816042, an amidine−imidazoline inhibitor of human factor Xa (FXa). The NMR experiments were performed on a lyophilized FXa−inhibitor complex. The complex was formed in solution in the presence of stabilizing excipients and frozen after gradual supercooling prior to lyophilization. The results indicate that the inhibitor binds with a distribution of orientations of the imidazoline ring.

Acute ischemia strikes sick and apparently healthy patients and precipitates heart attacks and strokes that greatly compound the initial tissue damage resulting from the temporary lack of blood supply. The majority of these episodes can be prevented or substantially ameliorated by drugs that inhibit or reverse blood-clot formation (*1*, *2*). Therefore, a major focus of pharmaceutical research has been antithrombotic agents that are targeted to inhibit specifically the trypsin-like proteinases of the blood coagulation cascade (*3*).

Human blood coagulating Factor Xa (FXa)[1] is a 45-kDa serine protease (*4*) that is structurally related to thrombin and trypsin (*5*). FXa has been an attractive target for the development of inhibitors because it acts early in the blood-coagulation cascade (*6*, *7*). Newly generated FXa forms a complex with Factor Va and Ca^{2+} on the exposed phospholipid of activated platelets or damaged cell membranes to constitute an active prothrombinase (*6*). This prothrombinase causes amplification of the coagulation response by converting a large pool of prothrombin into thrombin, which, in turn, promotes blood-clot formation by catalyzing the formation of fibrin from fibrinogen (*8*). This ultimately leads to the final step of the cascade in which fibrin is cross-linked into an insoluble plug (*6*).

The structure−activity-relationship approach to FXa−inhibitor construction by several research groups has consisted of connecting a central bridge to P1 and P4 moieties known to have selective affinity for the ionic S1 and hydrophobic S4 pockets of the similar trypsin, thrombin, and FXa serine proteases; modifications of lead compounds have then been screened for enhanced selectivity and potency for FXa inhibition (*9*). The expectation was that structural information would provide a rationale for compounds that showed pronounced selectivity for FXa over trypsin and thrombin.

However, early efforts at growing FXa crystals to assess inhibitor design by X-ray diffraction were problematic. Even after diffraction-quality FXa crystals were obtained following the removal of the 45 N-terminal residues of the γ-carboxyglutamic acid domain, the crystals were unsuitable for inhibitor-soaking experiments because the C-terminus of the A-chain occupied the active site of a FXa neighbor in a substrate-like manner. Inhibitor diffusion caused the crystals to crack (*3*, *10*). This problem led to the use of trypsin−inhibitor complexes for FXa-inhibitor evaluation, with the advantage of high throughput due to reliable crystallization conditions and quality crystals. Because of this advantage, trypsin became an important model system for understanding FXa inhibition and cocrystallization results (*3*, *5*, *11*−*14*). An undesirable feature of this system is that crystal contacts can influence the binding modes of some FXa inhibitors (*3*). An example of extreme cocrystallization bias has recently been documented for an FXa inhibitor in a series patented by Zeneca. In this study, structures of trypsin with either normal or reversed inhibitor−enzyme orientations were found to depend on whether the crystals were orthorhombic or cubic, respectively (*14*).

Solid-state NMR does not demand the order imposed by a crystal lattice and so is not restricted to protein fragments, crystalline, or even microcrystalline samples. This means that the influence of protein−ligand dynamics and conformational heterogeneity is retained in samples examined by solid-state NMR. Analysis of protein binding sites by this method therefore avoids the potential bias arising from cocrystallization and has provided the insight to refine crystal structures where ligands were not present, or where electron density maps were weak and blurred in ligand binding sites (*15*−

† This work was supported, in part, by NIH Grant GM40634.

* Corresponding author. Phone: (314) 935-6844. Fax: (314) 935-4481. E-mail: schaefer@wuchem.wustl.edu.

‡ Washington University.

§ Present address: Department of Immunology and Pathology, Washington University School of Medicine, 660 S. Euclid Ave., St. Louis, Missouri 63110.

|| Berlex Biosciences.

[1] Abbreviations: ΔS, S_0-S, where S and S_0 are rotational-echo double-resonance signal intensities with and without dephasing pulses, respectively; FXa, human factor Xa; HEPES, *N*-[2-hydroxyethyl]-piperazine-*N*′-[2-ethanesulfonic]acid; REDOR, rotational-echo double resonance; TPPM, two-pulse phase modulation; PEG, poly(ethylene glycol).

10.1021/bi027369g CCC: $25.00
Published on Web 06/17/2003

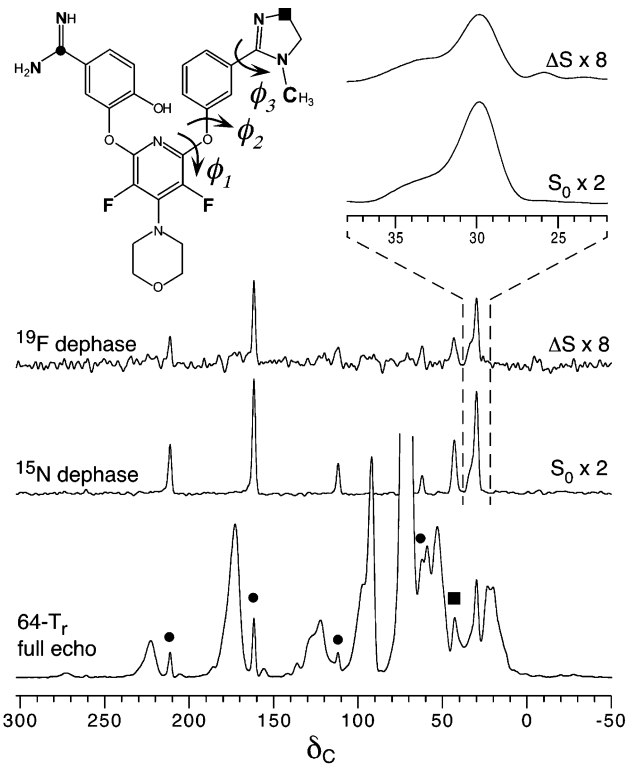

FIGURE 1: Double REDOR spectra of $^{13}C,^{15}N$-labeled ZK-816042 bound to FXa. The amidine sp^2 carbon (solid circle) and the methylene (solid square) and methyl carbons of the imidazoline ring are ^{13}C-labeled, and all four nitrogens of the amidine and imidazoline moieties are ^{15}N-labeled (inset, upper left). The full-echo spectrum after 64 rotor cycles of evolution is shown at the bottom of the figure. The peak that is off scale is due to carbons in the sugar lyoprotectant. The $^{13}C\{^{15}N\}$ REDOR difference spectrum (middle) had 16 rotor cycles of ^{15}N dephasing during 64 rotor cycles of evolution. Only signals arising from carbons with a directly bonded ^{15}N are observed. The ^{13}C natural-abundance background is eliminated. The methyl-carbon region of the spectrum shows two chemical-shift environments for the imidazoline methyl-carbon label (inset, top right). The $^{13}C\{^{19}F\}$ REDOR difference spectrum is shown at the top of the figure. Carbon−fluorine distances are determined using this spectrum as ΔS and the $^{13}C\{^{15}N\}$ REDOR difference spectrum as S_0. Magic-angle spinning was at 6250 Hz.

22). Perhaps the most germane example is our prior work with the symmetrical bisamidine FXa inhibitor (ZK-806299), in which we provided distance restraints to position both ends of a bisamidine inhibitor in the trypsin binding site (*23*).

In this paper, we extend our solid-state NMR work to the characterization of FXa inhibitors bound to nontruncated human FXa. Recently, a number of structures of FXa cocrystallized with arylamidine inhibitors have been solved (*7*, *12*, *24*, *25*). For Berlex compound ZK-816042 (see inset to Figure 1), the second amidine of the bisamidine ZK-806299 mentioned above is replaced by an imidazoline. The mixed amidine−imidazoline compound is a potent inhibitor of FXa ($K_I = 0.14$ nM) with 1700-fold selectivity for FXa over trypsin. The crystal structure of a similar bound inhibitor (ZK-807834; CI-1031, 183305-24-0) has sarcosine at the para position of the central pyridine ring rather than morpholine (see Figure 1). This compound differs from ZK-816042 (the compound we discuss in this paper) in bioavailability rather than potency (*26*). The crystal structure shows that the imidazoline apparently fits tightly into the hydrophobic S4 site of FXa with no salt-bridge formation (*24*). However, the results of $^{13}C\{^{15}N,^{19}F\}$ double REDOR experiments on a complex of ZK-816042 with FXa frozen from solution and lyophilized in a protective sugar matrix indicate a different conformation for the bound inhibitor than was anticipated based on the crystal structure of bound ZK-807834. The double REDOR results also indicate that the imidazoline moiety is locally disordered in the S4 site.

EXPERIMENTAL PROCEDURES

Formation of the Complex. ZK-816042 (see inset to Figure 1) was ^{13}C- and ^{15}N-labeled as described before (*27*); the fluorines are a natural part of the drug. The NMR sample was a 1:1 complex of human FXa with ZK-816042. With enzyme and inhibitor at 81.5 μM, the complex was formed in a lyophilization flask in a buffered 20 mL solution containing calcium and excipients with cryo- and lyoprotectant action (*28*). The solution was incubated at ice temperature and was then transferred to a low-temperature bath. After the sample temperature equilibrated at −4 °C, it was gradually cooled to −7 °C before ice crystal formation occurred. The flask was cooled to −80 °C in the bath before vacuum was applied to start lyophilization. The buffered solution contained the following excipients in 0.6 mM Ca-($C_6H_{12}NO_3S)_2$, 5 mM HEPES/NaOH, pH 7.4, PEG 8000 at 0.3125% (w/v) to protect the enzyme during freezing, 15 mM trehalose to protect the enzyme during drying, 0.67 mg/mL dextran (81.5 kDa) and 0.67 mg/mL dextran (488 kDa) to help prevent sample melt-back (*23*), as well as enhance stability of the solid-state sample (*29*). Buffer and excipient components were purchased from Sigma-Aldrich (St. Louis, MO). The FXa (75 mg) was obtained from Enzyme Research Laboratories (South Bend, IN).

Sample Lyophilization. After freezing, the NMR sample was initially lyophilized at reduced temperatures ranging from −80 to −30 °C until condensable vapor was no longer detected. Lyophilization was then continued as the flask temperature was raised in steps to room temperature. This procedure was part of a protocol we developed to prevent sample melt-back. Prior experiments in our laboratory indicated that melt-back of similar enzyme FXa inhibitor complexes could be prevented by the combination of dextran excipients with reduced flask temperatures during primary drying (*23*). Melt-back causes the cake to collapse during the primary drying, or ice sublimation, phase of lyophilization. A collapsed cake contains no voids. This undermines the efficiency of secondary drying, wherein liquid water is removed from the nonvolatile (protein/buffer/excipient) components of the cake, which are more accessible and present more surface area if voids created by ice sublimation have been preserved. Collapsed samples therefore have higher water content after the completion of drying (*30*). This has been shown to be problematic for the preservation of activity in a variety of proteins (*30*, *31*) and is relevant to extending the shelf life of protein pharmaceuticals (*31*). There is really not an issue with regard to removing too much water; secondary drying cannot remove tightly bound water from proteins without resorting to baking temperatures. Ideally, lyophilization preserves the protein with minimum retained water so that native structure is maintained in the solid state (*28*). Excess water can lead to protein denaturation and can increase the probability of unwanted chemical reactions that inactivate the protein during storage. In the

case of solid-state NMR, there is the issue of unwanted mobility with the plasticizer effect of higher water content. This can dramatically reduce signal intensity in a cross-polarization experiment. We are also, of course, concerned about sample stability before, during, and after NMR experiments. We have the benefit of ideal storage and handling. Our samples are packed in rotors in a drybox, they are stored in freezers, and data is collected at subzero temperatures. Every aspect of this handling mitigates absorption of water, and it also serves to keep the sample below its glass transition temperature. In practice, we can return to samples months or years later to perform new experiments.

Lyophilization Apparatus. The lyophilizer was built from components. Except where specified, all vacuum hoses, valves, and fittings were manufactured by Varian vacuum products (Lexington, MA) from stainless steel (SS), except for the vacuum valves, which were made of corrosion-resistant nickel-coated brass. Varian KF flange connections were all made with SS centering rings equipped with Vitron O-ring seals. The following description of the apparatus starts with the vacuum source and ends the with lyophilization flask. Vacuum was produced by a two-stage rotary vane vacuum pump (Model 2004A; Alcatel Vacuum Products, Inc., Hingham, MS) filled with Blue Oil synthetic vacuum oil (ATR, Inc., Laurel, MD). The vacuum was protected against temporary power failure by a NW25 Vacuum Sentry valve (MKS Instruments, Boulder, CO). A NW25 zeolite molecular sieve foreline trap (MDC vacuum products division, Hayward, CA) protected the vacuum against oil backstreaming. Next, a NW25 manual vacuum valve was followed by a Hastings dual vacuum sensor connection (Teledyne Electronic Technologies, Hastings Instruments, Hampton, VA), a NW25 to NW16 reducer, a second manual valve, and a NW16 flexible SS vacuum hose. This was connected to a NW16 KF flange-fitted exhaust outlet of a custom-build SS coldfinger that was seated (with two O-ring seals) into the top of the polycarbonate cover of a HETO −115 °C mechanical cold trap (purchased from ATR, Laurel, MD). A second SS NW16 vacuum hose, connected to the trap inlet, led to a third manual vacuum valve, a third Hastings quick-change vacuum sensor connection, and finally, a third length of SS NW16 vacuum hose terminated by a 3/4 in. Virtis Quick-Seal valve. In practice, this Quick-Seal valve was connected in series using a second inverted Quick-Seal valve and two 3/4 in. adaptors to the silicon rubber top of a Labcono lyophilization flask. The second valve allowed us to remove the flask from the lyophilizer with its contents under vacuum, so dry samples could be transferred to a nitrogen drybox prior to sample packing. The vacuum sensors, each connected to a separate gauge, were purchased from Hastings Instruments. One is a model 2000, capable of measurements between 6×10^{-5} to 10^{+3} Torr; two are model 2002 sensors, capable of measurements between 1×10^{-4} and 10^{+3} Torr. Two sensors were placed between the foreline trap and cold trap. Because they were protected from condensable vapor, they reported the system vacuum. The third was mounted near the flask to monitor the progress of lyophilization by detecting the condensable vapor removed from the frozen solid. The Hastings quick-change valves allowed us to switch sensors between the flask and the system position if the flask sensor became fouled during a long lyophilization process. The final part of the apparatus consisted of a Neslab Endocal ULT-80 low-temperature bath circulator (Portsmouth, NH). This served for precise control of the shelf temperature of a frozen sample during lyophilization. We employed 95% ethanol as a bath-circulator coolant for operation between −85 and +10 °C. The lid to the 4-gallon SS reservoir was replaced with a block of alcohol-proof plastic bolted in place with an O-ring seal. Two circular openings were machined into this block, and adaptors were invented to allow the immersion of either 300 mL or the smaller 50−80 mL Labcono lyophilization flasks directly into the reservoir tank. A spring-loaded restraint held the flask in place, using the lower outside edge of the silicone cap on the lyophilization flask or an O-ring seal on a dummy Teflon cap to protect the coolant from absorption of atmospheric water during use.

REDOR and Double REDOR. REDOR was used to restore the dipolar couplings between heteronuclear pairs of spins that are removed by magic-angle spinning (*32*). REDOR experiments are always done in two parts, with rotor-synchronized dephasing pulses (S) and without (S_0). The dephasing pulses change the sign of the heteronuclear dipolar coupling, and this interferes with the spatial averaging resulting from the motion of the rotor. The difference in signal intensity ($\Delta S = S_0 - S$) for the observed spin in the two parts of the REDOR experiment is directly related to the corresponding distance to the dephasing spin (*33*). REDOR has found application in the characterization of binding sites of proteins (*15*−*23*, *34*, *35*) and in the analysis of heterogeneous biological materials such as amyloid plaques (*36*), membrane protein helical bundles (*37*), insect cuticle (*38*), bacterial cell walls (*39*), and spider silk (*40*).

Double REDOR consists of two separate REDOR experiments performed sequentially (*41*). The first REDOR sequence (see Figure 2 of ref *41*) is designed to remove interferences from the natural-abundance ^{13}C background. If the ^{13}C labels are introduced with a ^{15}N directly bonded partner, then the $^{13}C\{^{15}N\}$ ΔS (for a short dipolar evolution period) arises just from the ^{13}C labels. (The nucleus outside the curly bracket in this notation is the observed spin, and the nucleus inside the bracket is the dephasing spin.) This spectrum becomes the reference for a measurement of the coupling to a third label, typically ^{31}P or ^{19}F. The latter was used in ZK-816042 and $^{13}C\{^{19}F\}$ REDOR dephasing therefore measured $^{13}C-^{19}F$ dipolar coupling with no background corrections necessary. In both REDOR experiments, a single ^{13}C refocusing pulse was used to avoid possible ^{13}C-^{13}C recoupling in the multi-^{13}C labeled samples. This protocol has the advantage of avoiding possible phase twists in the ^{13}C spectrum after long evolution times but the disadvantage of no phase alternation of the ^{13}C π pulse to avoid the effects of pulse imperfections (*42*). The same double REDOR strategy has been used recently to determine the conformation of a ^{13}C,^{15}N,^{19}F-labeled paclitaxel bound to bovine microtubules (*43*).

Spectrometer. REDOR NMR was performed using a 6-frequency transmission-line probe (*44*) having a 12-mm long, 6-mm inside diameter analytical coil, and a Chemagnetics/Varian ceramic stator. Lyophilized samples were contained in thin-wall Chemagnetics/Varian 5-mm outside diameter zirconia rotors. The rotors were spun at 6250 Hz with the speed under active control to within ±2 Hz. A stack-mounted air chiller cooled the rotor to an exit-gas temperature

of −10 °C. The spectrometer was controlled by a Tecmag pulse programmer. Radio frequency pulses for ^{13}C (125 MHz) and ^{15}N (50.7 MHz) were produced by 1 and 2-kW American Microwave Technology power amplifiers, respectively. Proton (500 MHz) and ^{19}F (470 MHz) radio frequency pulses were generated by 1-kW Amplifier Systems tube amplifiers driven by 50-W American Microwave Technology power amplifiers. The π-pulse lengths were 10 μs for ^{13}C and ^{15}N and 5.0 μs (40 T_r) or 5.7 μs (32, 48, 56, and 64 T_r) for ^{19}F. Standard XY-8 phase cycling (*42*) was used for all dephasing pulses. A 12-T static magnetic field was provided by an 89-mm bore Magnex superconducting solenoid. Proton−carbon cross-polarization transfers were made in 2 ms at 50 kHz. Proton dipolar decoupling was 100 kHz during data acquisition; TPPM of the ^1H radio frequency (*45*) was used throughout both dipolar evolution and decoupling periods.

REDOR Calibration. The accuracy of distance measurements using a single ^{13}C refocusing pulse (to avoid phase twists in the ^{13}C spectra) and many ^{19}F-dephasing pulses was estimated using the two-bond coupling of [^{19}F]polycarbonate (*46*, *47*). The anisotropy of the ^{19}F chemical-shift tensor in this material is about 50 kHz (at 470 MHz), which is close to that of the ^{19}F labels in ZK-816042. The isolated-pair $^{13}C-^{19}F$ dipolar coupling in [^{19}F]polycarbonate is 2068 Hz, which leads to full dephasing in four rotor cycles (4 T_r) with magic-angle spinning at 6250 Hz. This was a 6-T_r experiment with a single ^{13}C refocusing pulse at 3 T_r and ^{19}F dephasing pulses at 1/2, 1, 3/2, 2, 4, 9/2, 5, and 11/2 T_r. The middle two rotor periods are used for refocusing chemical shifts and do not contribute to dipolar dephasing. In a corresponding 6-T_r test experiment with the same ^{13}C refocusing pulse at 3 T_r, but the ^{19}F dephasing pulses now at 1/4, 3/4, 5/4, 7/4, 17/4, 19/4, 21/4, and 23/4 T_r, no dephasing is expected (*33*). However, this is true only if the sign reversals of the π pulses on both ^{13}C and ^{19}F channels are exactly matched. The presence of a difference signal in the test experiment is therefore a direct measure of the diminution of REDOR dephasing (*48*) resulting solely from the summed effect of all ^{13}C and ^{19}F pulse imperfections (*49*). A diminution of dephasing results because full dephasing can only be achieved if there is an exact reversal of the sign of the dipolar coupling with each π pulse. The measured signal in the test experiment was 17% of S_0. The same diminution was measured for full 2-kHz $^{13}C-^{19}F$ dipolar coupling and eight dephasing pulses as for 500-Hz $^{13}C-^{19}F$ dipolar coupling and 32 dephasing pulses. In the latter case, a reduction in effective dipolar coupling (D_{eff}) was achieved by reducing the spacing between the ^{19}F dephasing pulses within a rotor period (*33*). This result shows that for evolution times less than that required to produce full dephasing, the diminution depends linearly on $D_{eff}T_r$. These corrections are not necessary if it is possible to use equal numbers of ^{13}C and ^{19}F π pulses and *xy*-8 phase cycling on both channels. That is, quantitative $^{13}C\{^{19}F\}$ REDOR is better done on samples with low concentrations of ^{13}C. Additional details will be published elsewhere (*49*). All observed $^{13}C\{^{19}F\}$ REDOR differences for complexes of ZK-816042 were increased by 17% in plots of $\Delta S/S_0$. Failure to make this correction would lead to an overestimate of a C−F distance by approximately 5%.

REDOR Model. For each carbon label, the $^{13}C-^{19}F$ dipolar couplings (and the corresponding distances) were determined by comparisons of the corrected $^{13}C\{^{19}F\}$ REDOR $\Delta S/S_0$ intensities to those calculated using multi-spin simulations and assumed inhibitor geometries (*23*). The dipolar coupling constant was reduced from the rigid-lattice values by 7% in the calculations, 5% because of ultrafast vibrational averaging (*29*, *37*), and 2% because of $^{19}F-^{19}F$ interactions, the latter revealed by simulations using SIMPSON (*50*) with and without F−F homonuclear coupling. The distances for the best match of simulated and experimental dephasing characterized the conformation of the inhibitor in the binding site, a conformation referred to as the REDOR model. This model has no specific information about the binding site itself.

REDOR-Refined X-ray Model. A second model was constructed of ZK-816042 bound to FXa using molecular dynamics simulations with REDOR distance constraints. The published coordinates of the FXa/ZK-807834 complex (PDB code 1FJS, ref *24*) were used as starting coordinates for FXa. Atoms further than 12 Å from the inhibitor were fixed, and successively weaker harmonic restraints were used from 12−4.5 Å from the inhibitor. Only the Cαs were restrained for residues closer than 9.0 Å. Ten sets of initial coordinates were generated for ZK-816042 by hand manipulation. The benzamidine group remained fixed in the S1 pocket. The imidazoline group was rotated and placed in the vicinity of Trp215 (S4 pocket), Ser195 (S1′ pocket), or packed over the backbone residues of Glu217. The starting coordinates of the inhibitor were then randomized by ±1 Å. Approximately 500 structures were generated by 2400 steps (1.2 ps) of simulated annealing from 800 to 300 K, followed by energy minimization using XPLOR 3.1 (*47*). No solvent was used in these calculations, and the inhibitor was uncharged. The REDOR distance restraints were introduced using a sequentially stronger harmonic potential peaking at 6 kcal/Å^2. The salt bridge between the benzamidine and Asp189 was also enforced by distance restraints. The structure with the lowest energy for the inhibitor of all the structures that satisfied the distant constraints is referred to as the REDOR-refined X-ray model. This model is distinct from the REDOR model.

RESULTS

REDOR Dephasing, Carbon−Fluorine Distances, and the REDOR Model. The ^{15}N labels of ZK-816042 were positioned to select three specific ^{13}C-labeled carbons in a $^{13}C-\{^{15}N\}$ REDOR experiment. This established full-echo ^{13}C S_0 intensities (see Figure 1, middle spectrum) with no interferences from the natural-abundance ^{13}C background (*23*, *41*). The amidine-carbon $^{13}C\{^{19}F\}$ dephasing (Figure 1, top) and dipolar coupling are not reduced because of averaging by large-amplitude molecular motion (*23*), as revealed by the full-intensity chemical-shift spinning sidebands (Figure 1, middle). A minor $^{13}C\{^{19}F\}$ difference peak at 175 ppm is due to the proximity of the ^{19}F labels to natural-abundance ^{13}C in the FXa peptide carbonyl carbons.

The observed $^{13}C\{^{19}F\}$ dephasing for the carbon labels is substantially less than that predicted from the conformation of the X-ray structure for the phenoxy rings about the central pyridine of ZK-807834 (Figure 2). As a result, the crystal structure proximal $^{13}C-^{19}F$ distance is 7.1 Å for the imidazoline methylene carbon and 7.8 Å for the methyl

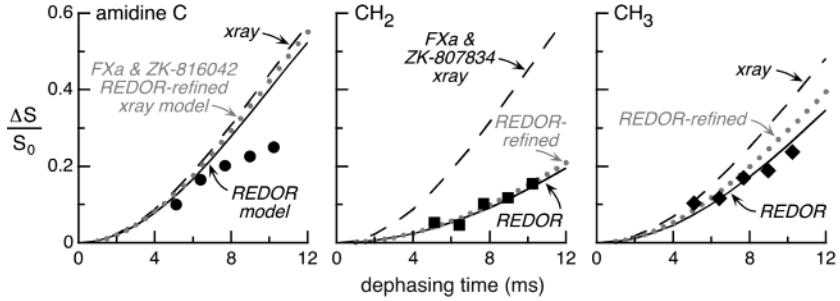

FIGURE 2: $^{13}C\{^{19}F\}$ REDOR dephasing ($\Delta S/S_0$) based on double REDOR spectra of $^{13}C,^{15}N$-labeled ZK-816042 bound to FXa. Experimental values are shown by the solid symbols. Errors estimated by the scatter are less than 10%. Calculated values (solid lines) for the dephasing of the methylene and methyl carbons of the imidazoline ring (middle and right panels) were matched to the experimental dephasing arising from two ^{13}C-^{19}F dipolar couplings by varying the orientation of the imidazoline-ring moiety about the central phenoxy ring (see inset to Figure 1). A best fit was found for $\varphi_1 = 53°$, $\varphi_2 = 70°$, and $\varphi_3 = 94°$. The corresponding angles in the crystal structure of ZK-807834 are 115, 327, and 88°, respectively. Both methylene and methyl-carbon calculated dephasings were insensitive to rotations about φ_3. The amidine-ring moiety was positioned in the S1 binding site as described in ref *52*. The REDOR model and X-ray structures in the S1 site are virtually superimposable, and calculated REDOR dephasing for the two are similar (left panel) and in reasonable agreement with experiment (solid circles) through 8 ms of dephasing. The calculated dephasing for the X-ray structure of Figures 3 and 4 is shown by dashed lines and that for the REDOR-refined X-ray model of Figure 4 by dotted lines.

Table 1: Selected $^{13}C-^{19}F$ Distances for Labeled[a] ZK-816042 Bound to Human FXa

	Proximal F (Å)		Distal F (Å)	
carbon	X-ray[b]	REDOR[c]	X-ray[b]	REDOR[c]
methyl	7.8	8.3	11.2	9.5
imidazoline CH_2	7.1	9.3	11.7	11.5

[a] See Figure 1 (inset, top left). [b] From ref *24* for ZK-807834. [c] This paper.

carbon, whereas the corresponding REDOR experimental distances are 9.3 and 8.3 Å, respectively (Table 1). Thus, the REDOR structure has the methyl group closer to the fluorines of the central ring than the methylene carbon, opposite to the positioning of the X-ray structure. The longer $^{13}C-^{19}F$ distances detected by REDOR probably result from rotations about the flexible Ar−O−Ar bonds (Figure 1, insert, top left; and Figure 2, caption). These values indicate a U-shape for the two arms flanking the central ring rather than the L-shape of the crystal structure (Figure 3).

We assumed that the amidine moiety of ZK-816042 was positioned in the S1 binding site by analogy with the X-ray structure of ZK-807834 and other REDOR-determined structures for amidine inhibitors of FXa (*23*, *52*). The distances from the amidine carbon to the fluorines in the REDOR model of Figure 2 are 7.6 and 9.8 Å, somewhat greater than the 7.4 and 9.3 Å values of the X-ray structure. This increase results in slightly less dephasing than predicted by the X-ray structure (Figure 2, left panel). The dephasing predicted by both the REDOR model and the X-ray structure is in reasonable agreement with experiment, at least through 8 ms of dipolar evolution. For longer dephasing times (48 and 56 T_r), the observed dephasing is less than expected. This may be the result of amplifier droop and imperfect π pulses. Only the 40-T_r experiment (and the REDOR calibration) used a 5-μs ^{19}F π pulse (see Experimental Procedures). The decrease in dephasing may be more pronounced for the amidine carbon than for the imidazoline carbons because both ^{13}C and ^{19}F shift tensors are large for the amidine carbon. The effects on REDOR dephasing of variations in both phase and amplitude during π pulses are difficult to calculate but probably are greater for carbons with large shift tensors.

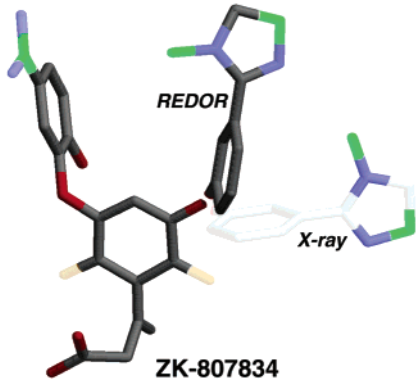

FIGURE 3: Comparison of the REDOR-based structure of ZK-816042 bound to FXa (from Figure 2), with the crystal structure of ZK-807834 bound to FXa. The morpholine ring of ZK-816042 is not shown. The REDOR model is shown in dark gray, with ^{13}C in green. The X-ray structure is shown in white, with ^{15}N in purple and ^{13}C in green. The two fluorines of the central ring are shown in yellow.

Because tight binding and salt-bridge formation at the S1 site are not in doubt, no attempt was made to alter the REDOR model to improve the match between calculated and experimental dephasing for the amidine carbon. The conclusion in the preceding paragraph that the REDOR dephasing for the imidazoline carbons is inconsistent with the X-ray structure depends primarily on relative dephasing rates (more dephasing for the methyl carbon than for the methylene carbon) and not on absolute distance determinations.

The expansion in the inset to Figure 1 (top right) shows two isotropic chemical shifts for the imidazoline methyl carbon, one at 30 ppm and the other at about 33 ppm. This result indicates that there are at least two major chemical environments for the imidazoline methyl carbon, with the 30-ppm environment higher in concentration by a ratio of about 3:1. These environments are likely the result of two preferred values for the φ_3 rotation angle shown in the inset (top left) to Figure 1. However, the 3-ppm methyl-carbon line widths also suggest a distribution of isotropic shifts associated with distributions of angles about the preferred values of φ_3. No attempt was made to distinguish differences in dephasing for the two methyl environments because of sensitivity limitations.

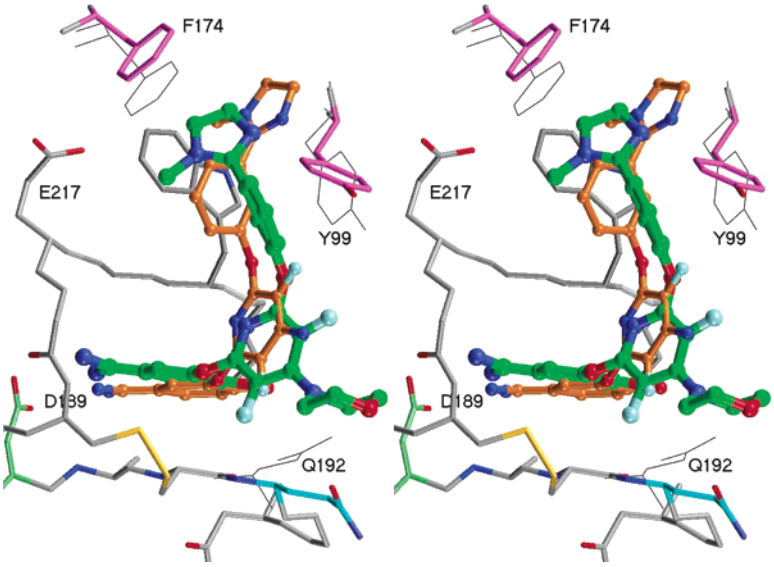

FIGURE 4: A stereoview of the calculated structure for ZK-816042 bound to FXa (the REDOR-refined X-ray model). This model is derived using the REDOR distance restraints of Table 1. The inhibitor is shown as a ball-and-stick figure with green carbon atoms. Superimposed on this structure is the X-ray structure of FXa/ZK-807834. ZK-807834 appears as a slightly smaller ball-and-stick figure with orange colored carbon atoms. Most of the sarcosine group has been removed from ZK-807834 to simplify the view. A few key FXa residues from the crystal structure are shown as wire frames. Trp215 is behind the green imidazoline ring.

REDOR-Refined X-ray Model. The REDOR distance restraints imposed during molecular dynamics simulations reduced the gap between the amidine carbon and the methyl group on the imidazoline from 10.7 Å (observed in the X-ray structure of ZK-807834, 1FJS, ref *24*) to 8.3 Å. The resulting change in conformation of the inhibitor improves the fit between calculated and experimental REDOR dephasing to an acceptable level (Figure 2) but does not match the quality of the fit provided by the REDOR model. The change in conformation forces a rearrangement of the inhibitor in the binding site (Figure 4). The central pyridine ring shifts away from the Cα of Trp215 by 1 Å. The imidazoline ring moves toward Glu217 by 3 Å and away from Try99. The phenoxy linker that connects the imidazoline ring to the central pyridine ring has also shifted as compared to the corresponding group in ZK-807834. It now points toward the solvent and has lost contact with Trp215. The root-mean-squared deviation of the atomic coordinates of the inhibitor was 0.5 Å. This measurement was based on the five best structures that had the imidazoline ring bound in the S4 pocket.

Figure 4 also shows that several residues in the protein have been displaced. The side chain amine of Gln192 shifts by 2.5 Å to accommodate the morpholine ring of the inhibitor. Comparison to the X-ray structure indicates that this motion would displace a water (#638) from the binding site. The movement of the imidazoline ring causes several residues to shift in the S4 pocket. Phe174 moves back by 1.3 Å. The shift of the imidazoline ring leaves the indole ring of Trp215 exposed to the solvent. The phenol side chain of Tyr99 rotates by 60° to cover the exposed aromatic group. The overall packing in the S4 pocket is similar to what was seen for published structures of RPR208707 and RPR208815 in FXa (1F0S and 1F0R, respectively, ref *7*).

The structural calculations also revealed a second conformation for ZK-816042 that fit the experimental data. In this second conformation, the imidazoline ring is shifted out of the S4 pocket and placed in close contact with Glu217. A similar conformation has been observed in early theoretical models for other compounds from this template (unpublished). However, there is no precedent for this conformation from other structural work. Furthermore, recent work from a benzothiophene template has shown that neutral substitutions for the S4 substituent still retain subnanomolar potency (*53*). Therefore, this second conformation was rejected.

DISCUSSION

REDOR Model. The REDOR model of Figure 3 suggests that ZK-816042 adopts a U-shape rather than an L-shape conformation in the binding site of FXa. While this conclusion may be considered speculative because the REDOR model takes no account of the energetics of the inhibitor and protein within the binding site, the disorder observed in the S4 binding site (Figure 1, top right insert) is not speculative. This disorder is not compatible with the notion that the subnanomolar binding of ZK-816042 is due to a tight fit at both salt-bridge (S1) and hydrophobic (S4) binding sites. It is possible that the high affinity is the result of a tight fit only at the S1 site (note the narrow amidine-carbon lines in Figure 1) with local disorder at the S4 site. By this view, the combination of an exothermic enthalpic contribution to free energy at S1, and only a modest entropic free energy penalty at S4, generates the observed K_I. The REDOR model can accommodate inhibitor heterogeneity at the S4 site because of the insensitivity of the $^{13}C\{^{19}F\}$ dephasing of the imidazoline ^{13}C labels on φ_3 (see caption to Figure 2).

REDOR-Refined X-ray Model. Figure 4 shows the REDOR-refined X-ray model of ZK-816042 superimposed on the X-ray structure of the binding site containing ZK-807834 (1FJS, ref *24*), a nearly identical compound from the same template. Both inhibitors share the same overall conformation. The benzamidine group of each compound forms a salt bridge with Asp189, and the basic imidazoline ring occupies the S4 binding pocket. The X-ray structure, and the REDOR-refined X-ray model built from the X-ray structure, each show only a single conformation for the inhibitor. However,

as mentioned above, the REDOR data clearly indicate that there are multiple conformations for the imidazoline group in the S4 pocket. This discrepancy may simply be the result of the inherent insensitivity of the X-ray experiment to structural heterogeneity.

Each X-ray reflection pattern sums the scattered X-ray intensity from every atom in the crystal lattice. Therefore, the final structure represents an average over all the conformational states of the protein. However, without high-resolution data (<1.8 Å), it is difficult to distinguish multiple binding conformations of the inhibitor. Nevertheless, information about the flexibility of the inhibitor is encoded in the *B*-factors of the atoms. Elevated *B*-factors usually correlate with conformational flexibility and structural heterogeneity. The *B*-factors for most atoms in the inhibitor (29 Å^2) are significantly higher than those for the atoms in the S1 pocket (17 Å^2). In addition, protein atoms within the S4 pocket also show elevated *B*-factors. Furthermore, comparisons between the 10 different X-ray structures for FXa/inhibitor complexes (*7*, *12*, *24*, *25*, *52*) show that there are considerable variations in the covalent structure of the S4 substituent and the linker to the S1 pocket. No single interaction with the protein is conserved among these inhibitors outside the S1 pocket. Taken together, these results suggest that any single FXa inhibitor may have multiple S4 binding modes, even though only single conformations are shown for the inhibitors in Figure 4.

REDOR and X-ray Samples. Apart from structural heterogeneity primarily because of rotational flexibility of the imidazoline ring about φ_3, there are other measurable differences between the two inhibitor conformations of Figure 4 that deserve further discussion. In particular, the REDOR-refined X-ray model does not have as pronounced an L-shape conformation as does the X-ray structure, although it is not as clearly U-shaped as the REDOR model of Figure 3. If more residues of the binding site were allowed to move during the REDOR-restrained calculation, the resulting shape of the inhibitor might be closer to that of the REDOR model.

It seems unlikely that crystal-packing forces altered the conformation of the inhibitor to account for its L-shape. For the X-ray structure of the FXa/ZK-807834 complex (1FJS, ref *24*), the active site of the protein faces a large cavity inside the crystal lattice. The closest contact to a symmetry-related protein is over 10 Å away. Furthermore, the L-shape binding conformation for ZK-807834 has been observed for many different FXa inhibitors, including those whose structures were determined from different crystal forms (*25*, *52*). We are led to the conclusion that the differences in inhibitor conformations between the two models and the X-ray structure may result from genuine differences between the samples examined in the NMR and X-ray experiments.

It is possible that the solutes used in the crystallization perturbed the structure. There is some unexplained electron density above the phenoxy linker in the S4 pocket for 1FJS (Adler and Whitlow, unpublished results). This density resembles an aliphatic chain and has been observed in the crystal structures of several FXa inhibitors from this template and from a benzothiophene template. The crystals were grown in 15−21% PEG-1500, and several small sugar-like solutes were also used as cryoprotectants. The results indicate that an aliphatic chain from a solute molecule may have stabilized the conformation of the inhibitor by covering the solvent-exposed surface of the phenoxy linker. The inhibitor may adopt a different conformation when these solutes are absent.

On the other hand, it is also possible that the conformation of the inhibitor was perturbed during the preparation of the sample for solid-state NMR. Previous results have demonstrated that native structures of an enzyme−inhibitor complex are preserved under the conditions used during lyophilization (*17*, *54*). However, the ligands in both those studies were held in place by ionic interactions with the protein. ZK-816042 has a large solvent-exposed surface. Only the benzamidine ring in the S1 pocket is held in place by hydrogen bonds. The conformation of the inhibitor may therefore have been perturbed by the removal of water during lyophilization despite the presence of stabilizing sugars. Notably, the structure shown in Figure 4 indicates that the inhibitor would displace at least one water from the active site (#638 in 1FJS). Sample heterogeneity may have been introduced at this point. Experiments using ^{17}O labeled water are planned to assess the retention of binding-site water during lyophilization.

We are left with an unanswered question raised by the differences in the bound conformations for the inhibitor shown in Figures 3 and 4. The weak dephasing for the ^{13}C labels in the imidazoline ring (Figure 2) proves that there are substantive differences (not just involving rotations about φ_3) between the NMR models and the X-ray structure. Assuming that these differences are due to the special conditions of the sample preparations for the two experiments, we are unable to say which preparation most faithfully represents the conformation of the inhibitor in the occupied binding site of FXa in solution.

ACKNOWLEDGMENT

The multi-spin simulations were done with software generously supplied by the laboratory of Prof. Niels Chr. Nielsen (University of Aarhus).

REFERENCES

1. Moons, A. H. M., Levi, M., and Peters, R. J. G. (2002) *Cardiovasc. Res. 53*, 313−325.
2. Weir, B., Macdonald, R. L., and Stoodley, M. (1999) *Acta Neurochir. Suppl. (Wien) 72*, 27−46.
3. Renatus, M., Bode, W., Huber, R., Sturzebecher, J., and Stubbs, M. T. (1998) *J. Med. Chem. 41*, 5445−5456.
4. Lawson, J. H., Kalafatis, M. K., Stram, S., and Mann, K. G. (1994) *J. Biol. Chem. 269*, 23357−23366.
5. Whitlow, M., Arnaiz D., Buckman, B. O., Davey, D. D., Griedel, B., Guilford, W. J., Koovakkat, S., Liang A., Mohan, R., Phillips, G. B., Seto, M., Shaw, K. J., Xu, W., Light, D. R., and Morrissey, M. M. (1999) *Acta Crystallogr. D55*, 3557−3562.
6. Davie, E. W., Fujikawa, K., and Kisiel, W. (1991) *Biochemistry 30*, 10363−10370.
7. Maignan, S., Guilloteau, J. P., Pouzieux, S., Choi-Sledeski, Y. M., Becker, M. R., Klein, S. I., Ewing, W. R., Pauls, H. W., Spada, A. P., and Mikol, V. (2000) *J. Med. Chem. 43*, 3226−3232.
8. Mann, K. G., Nesheim, M. E., Church, W. R., Haley, P., and Krishnaswamy, S. (1990) *Blood 76*, 1−16.
9. Maignan, S., and Mikol, V. (2001) *Curr. Top. Med. Chem. 1*, 161−174.
10. Padmanabhan, K., Padmanabhan, K. P., Tulinsky, A., Park, C. H., Bode, W., Huber, R., Blankenship, D. T., Cardin, A. D., and Kisiel, W. (1993) *J. Mol. Biol. 232*, 947−966.
11. Dullweber, F., Stubbs, M. T., Musil, D., Sturzebecher, J., and Klebe, G. (2001) *J. Mol. Biol. 313*, 593−614.

12. Nar, H., Bauer, M., Schmid, A., Stassen, J. M., Wienen, W., Priepke, H. W., Kauffmann, I. K., Ries, U. J., and Hauel, N. H. (2001) *Structure (Cambridge) 9*, 29−37.
13. Stubbs, M. T., Huber, R., and Bode, W. (1995) *FEBS Lett. 375*, 103−107.
14. Stubbs, M. T., Reyda, S., Dullweber, F., Moller, M., Klebe, G., Dorsch, D., Mederski, W. W., and Wurziger, H. (2002) *Chembiochem. 3*, 246−249.
15. Hing, A. W., Tjandra, N., Cottam, P. F., Schaefer, J., and Ho, C. (1994) *Biochemistry 33*, 8651−8661.
16. Mueller, D. D., Schmidt, A., Pappan, K. L., McKay, R. A., and Schaefer, J. (1995) *Biochemistry 34*, 5597−5603.
17. McDowell, L. M., Barkan, D., Wilson, G. E., and Schaefer, J. (1996) *Solid State Nucl. Magn. Reson. 7*, 203−210.
18. McDowell, L. M., and Schaefer, J. (1996) *Curr. Opin. Struct. Biol. 6*, 624−629.
19. Klug, C. A., Lee, P. L., Lee, I.-S. H., Kreevoy, M. M., Yaris, R., and Schaefer, J. (1997) *J. Phys. Chem. 101*, 8086−8091.
20. Klug, C. A., Tasaki, K., Tjandra, N., Ho, C., and Schaefer, J. (1997) *Biochemistry 36*, 9405−9408.
21. Goetz, J. M., Poliks, B., Studelska, D. R., Fischer, M., Kugelbrey, K., Bacher, A., Cushman, M., and Schaefer, J. (1999) *J. Am. Chem. Soc. 121*, 7500−7508.
22. Mehta, A. K., Studelska, D. R., Fischer, M., Giessauf, A., Kemter, K., Bacher, A., Cushman, M., and Schaefer J. (2002) *J. Org. Chem. 67*, 2087−2092.
23. McDowell, L. M., McCarrick, M. A., Studelska, D. R., Guilford, W. J., Arnaiz, D., Dallas, J. L., Light, D. R., Whitlow, M., and Schaefer, J. (1999) *J. Med. Chem. 42*, 3910−3918.
24. Adler, M., Davey, D. D., Phillips, G. B., Kin, S.-H, Jancarik, J., Rumennik, G., Light, D. R., and Whitlow, M. (2000) *Biochemistry 39*, 12534−12542.
25. Kamata, K., Kawamoto, H., Honma, T., Iwama, T., and Kim, S. H. (1998) *Proc. Natl. Acad. Sci. U.S.A. 95*, 6630−6635.
26. Phillips, G. G., Buckman, B. O., Davey, D. D., Eagan, K. A., Guilford, W. J., Hinchman, J., Ho, E., Koovakkat, S., Ng, H. P., Post, J. M., Shaw, K. J., Smith, D., Subramanyam, B., Sullivan, M. E., Trinh, L., Vergona, R., Walters, J., White, K., Whitlow, M., Wu, S., Xu, W., and Morrissey, M. M. (1998) *J. Med. Chem. 41*, 3557−3562.
27. Guilford, W. J., Dallas, J., and Arnaiz, D. (2001) *J. Labeled Cpd. Radiopharm. 44*, 247−256.
28. Arakawa, T., Prestrelski, S. J., Kenney, W. C., and Carpenter, J. F. (2001) *Adv. Drug Delivery Rev. 46*, 307−326.
29. Allison, S. D., Manning, M. C., Randolph, T. W., Middleton, K., Davis, A., and Carpenter, J. F. (2000) *J. Pharm. Sci. 89*, 199−214.
30. Adams, G. D. J., and Ramsay, J. R. (1996) *J. Pharm. Sci. 85*, 1301−1305.
31. Breen, E. D., Curley, J. G., Overcashier, D. E., Hsu, C. C., and Shire, S. J. (2001) *Pharm. Res. 18*, 1345−1353.
32. Gullion, T., and Schaefer, J. (1989) *J. Magn. Reson. 81*, 196−200.
33. Gullion, T., and Schaefer, J. (1989) *Adv. Magn. Reson. 13*, 58−83.
34. Studelska, D. R., Klug, C. A., Beusen, D. D., McDowell, L. M., and Schaefer, J. (1996) *J. Am. Chem. Soc. 118*, 5476−5477.
35. McDowell, L. M., Schmidt, A., Cohen, E. R., Studelska, D. A., and Schaefer, J. (1996) *J. Mol. Biol. 256*, 160−171.
36. Balbach, J. J., Ishii, Y., Antzutkin, O. N., Leapman, R. D., Rizzo, N. W., Dyda, F., Reed, J., and Tycko, R. (2000) *Biochemistry 39*, 13748−13759.
37. Smith, S. O., Kawakami, T., Liu, W., Ziliox, M., and Aimoto, S. (2001) *J. Mol. Biol. 313*, 1139−1148.
38. Merritt, M. E., Christensen, A. M., Kramer, K. J., Hopkins, T. L., and Schaefer, J. (1996) *J. Am. Chem. Soc. 118*, 11278−11282.
39. Kim, S. J., Cegelski, L., Studelska, D. R., O'Connor, R. D., Mehta, A. K., and Schaefer J. (2002) *Biochemistry 41*, 6967−6977.
40. Michal, C. A., and Jelinski, L. W. (1998) *J. Biol. NMR 12*, 231−241.
41. Beusen, D. D., McDowell, L. M., Slomczynska, U., and Schaefer, J. (1995) *J. Med. Chem. 38*, 2742−2747.
42. Gullion, T., Baker, D. B., and Conradi, M. S. (1990) *J. Magn. Reson. 89*, 479−484.
43. Li, Y., Poliks, B., Cegelski, L., Poliks, M., Gryczynski, Z., Piszcek, G., Jagtap, P. G., Studelska, D. R., Kingston, D. G. I., Schaefer, J., and Bane, S. (2000) *Biochemistry 39*, 281−291.
44. Schaefer, J., and McKay, R. M. (1999) U.S. Patent 5 861 748.
45. Bennett, A. E., Rienstra, C. M., Auger, M., Lakshmi, K. V., and Griffin, R. G. (1995) *J. Chem. Phys. 103*, 6951−6958.
46. Wu, J., Xiao, C., Yee, A. F., Goetz, J. M., and Schaefer, J. (2000) *Macromolecules 33*, 6849−6852.
47. Goetz, J. M., Wu, J. H., Yee, A. F., and Schaefer, J. (1998) *Solid State Nucl. Magn. Reson. 12*, 87−95.
48. Chan, J. C. C., and Eckert, H. (2000) *J. Magn. Reson. 147*, 170−178.
49. Weldeghiorghis, T. K., and Schaefer, J. (2003) *J. Magn. Reson.*, in review.
50. Bak, M., Rasmussen, J. T., and Nielsen, N. C. (2000) *J. Magn. Reson. 147*, 296−330.
51. Brünger, A. (1993) X-PLOR: A System for X-ray Crystallography and NMR, Version 3.1, Yale University Press, New Haven, CT.
52. McDowell, L. M., McCarrick, M. A., Studelska, D. R., O'Connor, R. D., Light, D. R., Guilford, W. J., Arnaiz, D., Dallas, J. L., Poliks, B., and Schaefer, J. (2003) *J. Med. Chem. 46*, 359−363.
53. Adler, M., Kochanny, M. J., Ye, B., Rumennik, G., Light, D. R., Biancalana, S., and Whitlow M. (2002) *Biochemistry 41*, 12534−12542.
54. McDowell, L. M., Poliks, B., Studelska, D. R., O'Connor, R. D., Beusen, D. D., and Schaefer, J. (2003), *J. Biol. NMR*, in review.

BI027369G